

pubs.acs.org/JPCC Article

Electronic Structure of 1D Lepidocrocite TiO₂ as Revealed by Optical Absorption and Photoelectron Spectroscopy

Erika Colin-Ulloa, [⊥] Julia L. Martin, [⊥] Ryan J. Hanna, Michelle H. Frasch, Rebecca R. Ramthun, Hussein O. Badr, Joshua R. Uzarski, Michel W. Barsoum, Ronald L. Grimm,* and Lyubov V. Titova*



Cite This: J. Phys. Chem. C 2023, 127, 7275-7283



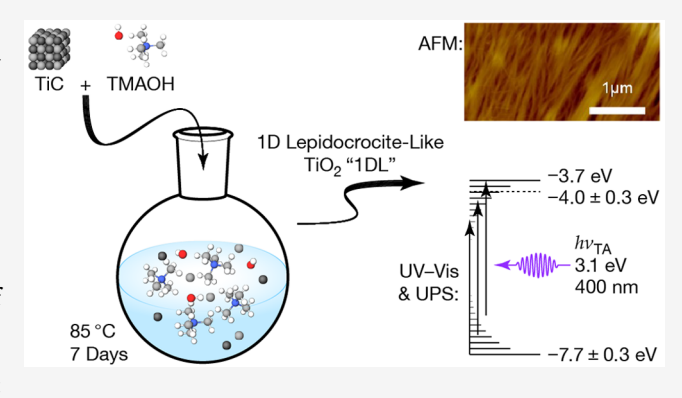
ACCESS I

III Metrics & More

Article Recommendations

s Supporting Information

ABSTRACT: We recently demonstrated scalable, one-pot syntheses of one-dimensional, titania lepidocrocite microfilaments by reacting Ti-containing water-insoluble, earth-abundant compounds such as TiC, TiB₂, TiN, etc., with tetraalkylammonium hydroxide, TMAOH, for a few days at 85 °C under ambient pressure. The resulting one-dimensional lepidocrocite (1DL) titania-based nanofilaments, NFs, tend to self-align along the [100] growth direction to form microfilaments that sometimes self-align into pseudo-two-dimensional (2D) sheets. With sub-square-nanometer cross sections, the resulting band gap energy, $E_{\rm g}$ at 4.0 eV is one of the highest ever reported for a titania material. Despite a large band gap, the nanofilaments exhibit significant absorbance throughout the visible spectrum ascribable to intra-gap defect



states based on UV–Vis absorbance data and ultraviolet photoelectron spectroscopy (UPS). UP spectra demonstrate work functions of 4.0 ± 0.3 eV vs vacuum and Fermi energies of 3.8 ± 0.1 eV with respect to the valence band edge. Transient absorption (TA) spectroscopy of the 1DL nanofilament thin films with sub-band-gap, visible-light illumination reveals photoexcitations with lifetimes in excess of nanoseconds. In combination with the established oxidative stability, long-lived visible photoexcitations bring forward possible applications of 1DL nanofilaments in photocatalysis and optoelectronics.

1. INTRODUCTION

Tackling global energy challenges requires inexpensive, nanostructured materials for a host of applications, including solar energy conversion via photocatalysis or generation of photocurrents in solar cells. Quite recently, we discovered a simple, one-pot, near-ambient, almost universal process to convert low-cost, ubiquitous nontoxic starting materials, such as TiC, TiN, TiB₂, and Mn₃O₄, into highly quantum-confined, oxidatively stable materials with excellent catalytic properties that are relevant to our global energy challenges.^{1,2}

Early studies have elucidated important phenomena in the synthesis and properties of these new materials. When utilizing titanium-based precursors, the resulting materials demonstrate nanometer-to-microns-long filaments with sub-nm² cross sections. More recently, we reported on the general validity of this synthesis protocol not only with Ti-based powders but also with Mn-bearing precursors that yield crystalline two-dimensional (2D) MnO₂ birnessite sheets with lateral sizes of ≈ 200 nm.² However, we presently focus on materials with Ti-based precursors. While initial density functional theory (DFT) calculations suggested a structure involving a one-dimensional (1D) analogue of anatase, more recent transmission electron microscopy (TEM) and Raman spectroscopy with updated calculations reveals a lepidocrocite-like one-

dimensional titania 1DL nanofilaments with sub-nanometer cross sections.³ Reports of lepidocrocite-like titania include its formation on templating surfaces such as Cu(001),⁴ as well as free-standing films,⁵ but this form is comparatively understudied relative to the anatase and rutile forms of TiO₂.

Precursors include TiC, TiB₂, TiN, Ti₃AC₂ (A = Al, Si, Ga, Sn, etc.), and Ti₂SbP that are immersed in an aqueous base at 85 °C for several days. The quaternary ammonium base may have propyl or butyl chains, but most commonly, we use tetramethylammonium hydroxide, TMAOH, that dissolves the precursor and, with time, results in the 1DL nanofilaments, the structure of which is shown in Figure 1.^{1,3} Interestingly, related investigations revealed that the sub-nanometer-wide products can self-assemble into a plethora of morphologies, from nanofilaments to bundles of nanofilaments, to micrometer-long filaments, and to two-dimensional flakes that are readily filtered into self-standing films.¹ Recent Raman and high-resolution

Received: September 20, 2022 Revised: March 16, 2023 Published: April 5, 2023





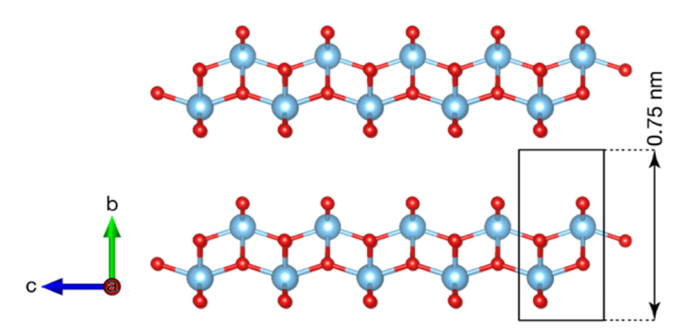


Figure 1. Schematic of nanomaterials composed of 1D lepidocrocite-like titanium dioxidedioxide, 1DL. Blue and red spheres represent Ti and O atoms, respectively. Adapted from ref 3.

transmission electron microscopy, TEM, studies of filtered films revealed the structure to be composed of 1DLs that are capable of self-alignment into pseudo-2D sheets. The 1DL NFs grow along the [001] and stack along the [010]. X-ray photoelectron spectra, XPS, and near-edge absorption spectra are consistent with the inclusion of both ${\rm Ti}^{3+}$ and ${\rm Ti}^{4+}$ oxidation states. ${\rm Ti}^{4+}$

Light absorption results from the initial report suggest a highly quantum-confined material. While researchers have previously produced 2D titania sheets with $E_g \approx 3.6 \text{ eV}$, to our knowledge, the $E_g = 4.0$ eV is the highest reported for titanium dioxide and remains consistent with quantum confinement effects as dimensions shrink.^{8,9} The strong quantum confinement effect that yields the increased band gap indirectly supports the 1D nature of our filaments and implies that the absorption axis is coupled to the sub-nm² cross section rather than their micron-scale lengths. While there is a wide body of literature that reports and discusses 1D anatase based on extremely high-aspect-ratio structures, as far as we are aware, our material is unique in showing substantial quantum confinement. Considering the sub-nanometer cross section, the 1DL nanofilamens possesses extremely high theoretical surface area of the order of $\approx 1000 \text{ m}^2 \text{ g}^{-1}$. Films of 1DLs demonstrate good performance as electrodes in lithium-ion and lithiumsulfur systems, as well as excellent oxidative stability. They are also quite good at photocatalytically producing hydrogen, H_2 . The latter results are particularly topical as nanostructured, 10,11 and doped^{12–15} titanium oxides are some of the most extensively investigated materials for photocatalytic and photoelectrochemical applications.

Despite promising initial results, questions remain regarding the specific chemical structure, surface states, and the interplay between those chemical features and the resulting electronic properties. Computational studies have postulated the properties of quantum-confined 1D titanium oxides; $^{16-19}$ however, few experimental reports exist on ultrathin titanium oxide with sub-nm thickness. Further, the large $E_{\rm g}=4.0$ eV band gap for the 1DLs stands in contrast to the material's dark color, which for $E_{\rm g}=3.0$ eV rutile and $E_{\rm g}=3.2$ eV anatase is frequently ascribed to be due to defects such as ${\rm Ti}^{3+}$ and oxygen vacancies. Significant sub-band-gap optical absorption in 1DL films supports the presence of defect states. The paucity of knowledge about 1DL combined with its catalytic potential drives research to understand the optical and electronic structure of this material and motivates the present investigation.

Herein, we synthesized 1DL from TiC and 25 wt % aqueous tetramethylammonium hydroxide, TMAOH, at 85 °C for 7

days. Solution-suspended 1DL nanofilaments were spin-deposited or drop-cast onto quartz for optical experiments or degenerately doped silicon for photoelectron spectroscopy. Atomic force microscopy (AFM) and transmission electron microscopy (TEM) established the morphology of our nanostructures. A combination of ultraviolet photoelectron spectroscopy (UPS) and UV–Vis spectroscopy elucidated electronic structure. Finally, transient absorption (TA) spectroscopy characterized optical excitations. We find that sub-gap 3.1 eV (400 nm) laser pulses generate long-lived photoexcitations with lifetimes in excess of nanoseconds, ns. This observation, combined with their high oxidative stability and exceptionally high surface area, suggests possible applications in water remediation, photocatalysis, and sensing, among many others.

2. EXPERIMENTAL DETAILS

2.1. Materials and Chemicals. Reagents for 1DL synthesis included TiC (99% pure, 2 µm gray powder, Strem, used as received) and tetramethylammonium hydroxide, TMAOH, (2.8 M or 25 wt % in water, Thermo Scientific, used as received). Post-synthesis treatment included lithium chloride (LiCl, >99%, ACS, Acros, as received), ethanol (anhydrous, histological grade, Fisher, as received), and >18 $M\Omega$ cm water (Millipore Milli-Q dispensing system). Chemicals for cleaning included concentrated sulfuric acid (H₂SO₄, ACS grade, Fisher, as received) and aqueous hydrogen peroxide (H2O2, 30%, Certified ACS, Thermo Scientific, as received). Quartz slides for optical spectroscopy experiments (Ted Pella) were cleaned with an Alconox solution, rinsed in water, and dried under argon, Ar (ultrahigh purity, Airgas). Silicon substrates for photoelectron spectroscopy experiments were single-sided polished, 525 \pm 15 μ m thick, $\leq 0.006 \Omega$ cm resistivity, degenerately arsenic-doped n⁺-Si(111) (Addison Engineering). Both quartz slides and silicon wafers were cleaned in piranha solution, rinsed in water, and dried under argon directly before use. Caution: piranha solution, a 3:1 mixture of concentrated H₂SO₄ and 30% H₂O_{2(ag)}, is a strongly oxidizing acid that reacts violently and exothermically with organic matter. Use appropriate safety measures for handling and disposal.

2.2. Synthesis of 1DLs and Film Preparation. Synthesis of 1DLs proceeded in capped 60 mL high-density polyethylene bottles (Nalgene). A 1/16'' hole was drilled in the bottle cap prior to use, affording venting during synthesis. Typical reagent quantities included 1.0 ± 0.03 g TiC and 10.3 ± 0.1 g TMAOH_(aq). The precursor quantities specified yield a 1:2.2 ratio between Ti metal atoms and TMA cations. With vigorous stirring from a cross-type stir bar, reactions proceeded for 7 days at 85 °C.

Following the synthesis, rinsing, purification, filtering, and deposition yielded the 1DL films under study. Centrifugation at 3000g for 2 min initially separated the particulate products from the TMAOH solution. Following decanting and discarding of the supernatant liquid, the 1DLs were resuspended in 15 mL of fresh ethanol via physical agitation and sonication. Three cycles of centrifugation as above, decanting, and resuspension further purified the material remaining in the pellet after each stage of rinsing and centrifugation in ethanol. Through each stage of ethanolic centrifugation, the supernatant showed no signs of suspended material and progressively transitioned from light brown to a clear solution. With the final decanting of the clear ethanolic

supernatant, the 1DL centrifugation pellet was suspended in 20 mL of water and thoroughly sonicated. Following centrifugation at 3000g for 2 min, the aqueous supernatant demonstrated significant turbidity that was decanted and utilized for ongoing film preparation while the centrifugation pellet was discarded. This aqueous suspension of 1DL nanofilaments was alternatively stored as non-LiCl-rinsed material or subsequently cleaned with LiCl to further remove any remaining tetramethylammonium, TMA⁺, cations.

For LiCl-rinsed 1DL films, we added 20 mL of 0.1 M $LiCl_{(aq)}$ to the turbid, aqueous supernatant suspension, agitated to mix, and sonicated the mixture for 30 min. Following sonication of the LiCl-containing 1DL suspension, centrifugation at 3000g for 2 min revealed a pellet that was retained and a clear supernatant solution that was discarded. Redispersion of the pellet in fresh water, sonication, and centrifugation at 3000g for 2 min yielded a turbid supernatant as above. This turbid supernatant was decanted and stored as a suspension of LiCl 1DLs while the pellet was discarded.

Films for AFM analyses were formed by spin coating a solution of 1 volume part 1DL suspension with 2 parts water onto quartz. Films for UV—Vis and transient absorption were deposited onto piranha-cleaned quartz from the 1DL supernatant suspension with no dilution. Films for photoelectron spectroscopy were drop-cast onto piranha-cleaned Si with no dilution.

2.3. X-ray Photoelectron Spectroscopy (XPS). A PHI 5600 XPS system, with a third-party data acquisition system (RBD Instruments, Bend, Oregon), acquired all photoelectron spectra, as detailed previously. The analysis chamber base pressures were <1 \times 10⁻⁹ Torr. A hemispherical energy analyzer, positioned at 90° with respect to the incoming monochromated Al K_{α} X-radiation, collected the photoelectrons. Analyses employed a 45° angle between the sample normal angle and both the X-ray source and the analyzer. Instrumental calibration included positioning Cu $2p_{3/2}$ at 932.67 eV and Au $4f_{7/2}$ at 84.00 eV on freshly sputter-cleaned samples that yielded Fermi-level positioning $E_{F,Au} \equiv 0.00 \pm 0.050$ eV.

The aforementioned thin films deposited on degenerately doped n-type Si substrates were mounted on freshly cleaned stainless steel pucks with Cu tabs and evacuated in the loading chamber for <1 h preceding direct transfer to the analysis chamber. Consistent binding-energy positions between samples and fitted Ti $2p_{3/2}$ features at ~459 eV obviated the need for charge neutralization in analyses of the films. In all experiments, survey spectra utilized a 117 eV pass energy, a 0.5 eV step size, and a 50 ms-per-step dwell time. High-resolution XP spectra employed a 23.5 eV pass energy, 0.025 eV step size, and a 50 ms dwell time per step.

Post-acquisition fitting utilized an in-house-developed Lab-VIEW-based program. Data fitting employed baseline-corrected, pseudo-Voigt, GL(x)-style functions, where x nonlinearly scales from a pure Gaussian (x=0) to a pure Lorentzian (x=100). Baseline functions were either of a linear type, a Shirley type, a Tougaard style with B=2900 eV² and C=1643 eV² within a universal function that is scaled to the height of the photoelectron data. Optimization routines utilize the built-in LabVIEW implementation of the Levenberg—Marquardt algorithm for multiparameter fitting. Fitting of the Li 1s, C 1s, and O 1s features utilized a Tougaard background and GL(30) functional peak shapes. The Li 1s region contained a neighboring Ti 3s feature as well as trace I

4d and Br 3d features that may be contaminants in the TMAOH solution. Spin-orbit-split doublets were individually constrained to have mutually identical full width at halfmaximum (fwhm) values for I 4d and Br 3d in that region. Fitting of the C 1s or O 1s regions necessitated multiple fit peaks. These peaks were constrained to have identical fwhm values, with the exception of the low-binding-energy C 1s feature centered at ~281 eV present on some samples, which was left unconstrained. A Tougaard background and GL(70) peak shapes described the Ti 2p features. The widths of Ti 2p doublets were constrained such that the width of each Ti 2p_{1/2} feature was 1.6× the width²⁶ and 0.5× the area of its corresponding Ti 2p_{3/2} feature based on high-resolution spectra of TiC and TiO₂ samples collected in-house. Si 2p and N 1s features utilize a linear background and GL(30) peak shapes. (We collected Si 2p to verify that the deposition substrate was not contributing to any spectral features that would interfere with the collection or interpretation of the UP spectra.) When present, Si 2p doublets were constrained to have identical fwhm values with the 2p_{1/2} peaks containing $0.5\times$ the area of the $2p_{3/2}$ peaks. Fitting of the N 1s region necessitated multiple fit peaks, and the fwhm values were left unconstrained.

2.4. Ultraviolet Photoelectron Spectroscopy (UPS). For UP spectra collected in the PHI 5600 chamber, a gas discharge lamp (UVS 40A2, Prevac, Rogów, Poland) generated the He I spectroscopic line, $E_{\text{He I}} = h\nu = 21.218 \text{ eV}$, from research-grade helium, He (Airgas). We utilized a -35 V substrate bias versus the grounded sample chamber to both maximize the desired spectral contributions of electrons from the sample and isolate unwanted secondary electrons from the analyzer. We chose the -35 V bias based on an invariance in spectral features and good linearity in analyzer response for UP spectra of a freshly Ar+-sputtered gold foil between biases of -20 and -50 V vs the sample chamber ground. As above, UP spectra of a freshly Ar⁺-sputtered gold foil verified instrumental calibration with the bias-corrected Fermi level of gold, $E_{F,A_{11}}$ 0.00 ± 0.05 eV. From plots of photoelectron counts vs biascorrected binding energy, the x-axis intercept of linear regressions quantifies a secondary electron cutoff energy, E_{SEC} , and a valence band-edge (maximum) energy, E_{VBM} . Considering the binding-energy calibration of the instrument, we report sample work function values, ϕ , as the difference between $\mathbf{E}_{\mathrm{He\ I}}$ and the secondary electron cutoff energy, or ϕ = $E_{\text{He I}} - E_{\text{SEC}}$. We report Fermi-level energies vs valence bandmaximum energies, or E_F – E_{VBM} . As ultrahigh vacuum bakeouts can yield a small perturbation in instrument calibration due to adsorbed contaminants changing the work function of instrument surfaces or the trajectory of photoelectrons between the sample and the hemispherical analyzer, both Au calibration and all 1DL data were acquired during the same "bakeout window."

2.5. UV-Vis Spectroscopy. A UV-Visible spectrometer (Evolution 300, Thermo Fisher Scientific, Waltham, MA) collected scattered light from drop-cast 1DL samples mounted in a Praying Mantis diffuse reflection accessory (Harrick Scientific Products, Pleasantville, NY) as well as transmitted light from 1DL samples mounted in a transmission-mode beam path. In both cases, films were deposited on 1" diameter-Piranha-cleaned quartz rounds utilizing the deposition protocol described above. Clean quartz served as the background reference for each scan. Directly preceding drop-cast film deposition, the quartz rounds were cleaned in a Piranha acid

solution, rinsed with Milli-Q water, and blown dry under an Ar stream. Scans were obtained in a range of 300–1000 nm, using a scan speed of 160 nm min⁻¹ and a bandwidth of 1 in absorbance mode.

- **2.6. Atomic Force Microscopy (AFM).** AFM imaging was carried out in no-contact mode using an atomic force microscope (NX20 Park Systems), with an Olympus cantilever OMCL-AC160TS. Images were recorded by Smart scan software (Park Systems) with a 5 \times 5 μ m² scan size and analyzed by XEI software (Park Systems).
- 2.7. Transmission Electron Microscopy (TEM). TEM samples were prepared by first diluting TiC-derived colloidal suspensions 1:300 in deionized (DI) water, then a few drops were drop-cast on a carbon-coated, lacey carbon, copper TEM grid (Cu-400LD, Pacific Grid Tech, San Francisco, CA). Samples were left to dry in a vacuum chamber at ambient temperature overnight before characterization. Imaging was acquired with field-emission TEM (JEOL JEM 2100F) at an acceleration voltage of 200 kV using a Gatan USC1000 CCD camera.
- 2.8. Transient Absorption (TA) Spectroscopy. The TA measurements were carried out using a HARPIA-TA Ultrafast Transient Absorption Spectrometer (Light Conversion). In the measurement, 1030 nm, 290 fs pulses from a ytterbium laser (Carbide, Light Conversion) generated probe white light through a sapphire crystal. An optical parametric amplifier (Orpheus, Light Conversion) generated 400 nm (3.10 eV) pump pulses. Pump-induced differences in absorption were detected in transmission mode by an Andor spectrograph and a Si photodiode array as a function of pump—probe delay time.
- **2.9.** X-ray Diffraction (XRD). A Bruker-AXS D8 Focus powder X-ray diffractometer with Cu K_{α} radiation collected X-ray diffraction (XRD) traces in the range of 5–45° (2 θ) at a step size of 0.05° and a dwell time of 5 s per step. X-ray tube operating conditions were 40 kV and 40 mA. Samples were drop-cast directly from the aqueous supernatant suspension onto a poly(tetrafluoroethylene) sample holder in successive steps to build up sufficient material for powder diffraction analyses.

3. RESULTS

In line with our previous work, present TEM (Figure 2A) and AFM (Figure 2B) images demonstrate the 1D character of many materials synthesized at 85 °C for 7 days. Individual, separated, long films yield highly aligned films with spin deposition (not shown) when imaged away from the axis of rotation, while drop casting yields disordered nanofiber porous films, as shown in the TEM image in Figure 2A. XRD traces for the films match previous reports, and are not discussed further.

Figure 2C shows the Tauc plot derived from a UV–Vis spectrum for a drop-cast film, for which Figure S1 in the Supporting Information section includes the corresponding raw UV–Vis data. Compared to spin deposition, drop casting yielded thicker films and easier UV–Vis analyses with a higher signal-to-noise ratio. Tauc construction demonstrates an onset of an indirect transition at \sim 4 eV, revealing the semiconducting nature of these structures. The films also exhibit an Urbach tail of sub-gap optical transitions covering the entire visible range. Note that $E_{\rm g}$ is significantly blue-shifted compared to bulk anatase TiO₂ (3.2 eV), likely because of strong quantum confinement of electrons in the 1D nanofilaments that are approximately 5 \times 7 Å² in cross section.

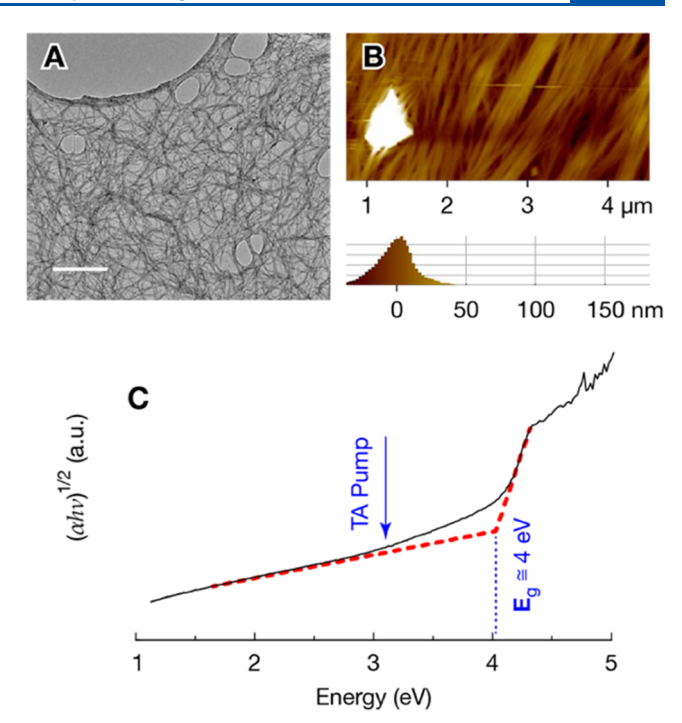


Figure 2. (A) TEM images from drop-cast 1DL porous films where the scale bar indicates 200 nm. (B) AFM image of spin-deposited film of 1DL with a histogram below that reflects the *z*-axis distribution of observed heights. (C) UV–Vis-spectroscopy-derived Tauc plots reveal an approximately 4 eV indirect band gap for drop-cast films. The arrow in (C) corresponds to the 3.1 eV energy of the optical pump pulses in transient absorption measurements.

However, a long sub-gap tail extending from the UV down to the near-infrared range shows that the photoresponse due to optical excitation in the visible spectrum is possible in these emerging nanomaterials. The aforementioned independence of UV—Vis absorption properties with deposition methods support that the observed behaviors are intrinsic to the 1DLs rather than emergent behaviors in the films.

Figure 3 presents representative XP spectra both (A) prior to and (B) following the LiCl rinse step that are consistent with previously published data. In Figure 3, we ascribe the red-shaded O 1s and Ti 2p features to the 1DL material itself. The Ti 2p_{3/2} feature occurs at 458.8–459.1 eV for all measured samples, which indicates that Ti⁴⁺ dominates, as previously observed. Green-shaded Ti 2p_{3/2} features at 455.2–455.3 eV and C 1s features at 281.8-282.0 eV are consistent with Ti²⁺ and reduced carbon that exist in the titanium carbide precursor. We conclude that a nominal amount of TiC precursor remains in some films, and we limit ourselves to quantifying films with <2% unreacted TiC as established by the Ti²⁺ to Ti⁴⁺ ratio of the Ti 2p_{3/2} features. Interestingly, accounting for one Ti4+ doublet and one Ti2+ doublet reveals another purple-shaded fittable doublet with Ti 2p_{3/2} at 457.0-457.8 eV, which is consistent with Ti³⁺ in the 1DL films. Observation of ${\rm Ti}^{3+}$ ascribable features is consistent with our previous results, 1 as well as preliminary electron-spin resonance experiments that will be the subject of upcoming studies. A notable blue-shaded N 1s feature at 403.7 eV in concert with a blue-shaded C 1s feature at 287.1 eV implies significant quantities of tetramethylammonium, TMA+, cations present prior to aqueous LiCl rinsing. The blue-shaded features of TMAOH cations largely disappear from the XP

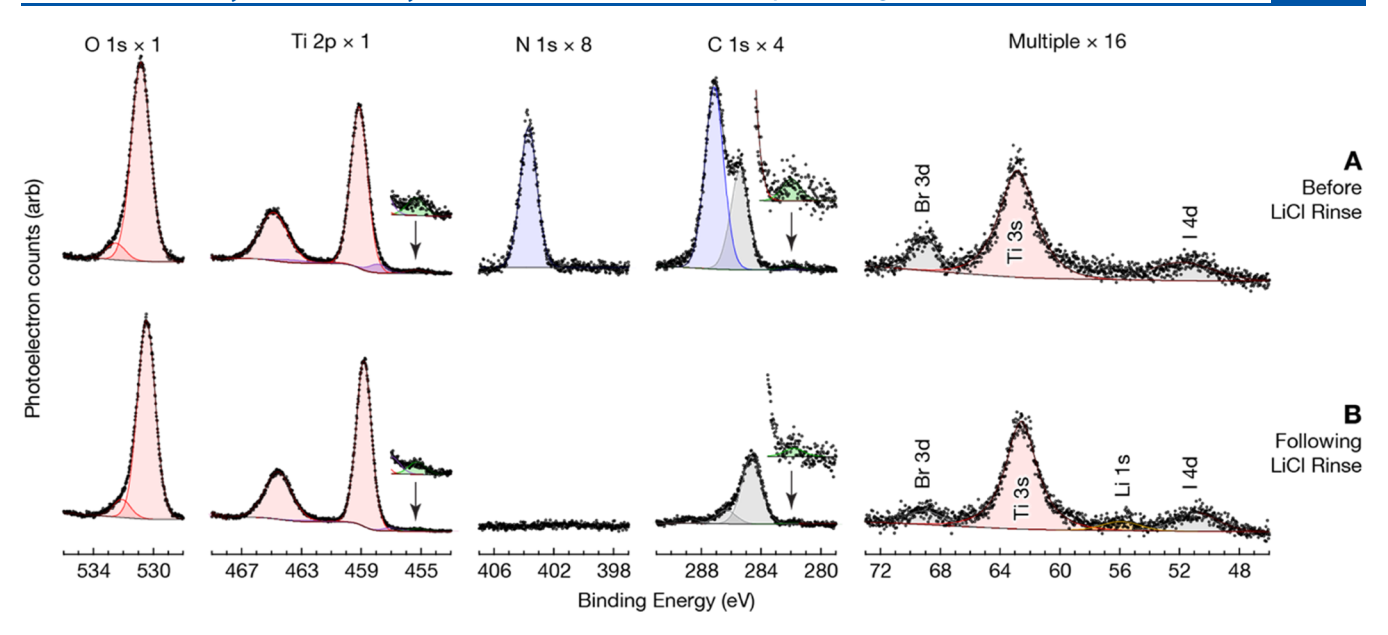


Figure 3. Representative XP spectra for drop-cast 1DL samples both (A) before, and (B) after LiCl rinsing. Red-shaded features are consistent with highly oxidized titanium oxides viz. Ti^{4+} , with trace purple-shaded features ascribable to Ti^{3+} at 457.0-457.8 eV. Green-shaded features and insets in the Ti 2p and C 1s region are consistent with the nominal TiC precursor. Insets represent a $\times 5$ zoom relative to their respective Ti 2p and C 1s regions. We ascribe blue-shaded features in panel (A) to residual TMA^+ cations that are exchanged with Li^+ cations duirng the LiClrinse that yields the orange-shaded Li 1s feature in panel (B). Gray-shaded features are ascribable to adventitious carbon species as well as Br^- and I^- contamination in the TMAOH reagent.

spectra following an aqueous LiCl rinse, while a demonstrable, green-shaded Li 1s feature appears at 55.9 eV. The carbon region further contains a gray-shaded feature at 284.6–285.4 eV that we ascribe to adventitious carbon contamination. In Figure 3B, we further ascribe the gray-shaded feature at 286.3 eV to oxidized adventitious carbon species rather than ammonium carbon due to the absence of N 1s fittable features following the LiCl rinse.

Figure 4 presents an ultraviolet photoelectron spectrum with a $\times 16$ inset of the Fermi region. We employed drop-cast films for UP spectroscopy to yield a sufficiently thick film to obviate spectral contributions from the Si substrate. Figure 3B displays the corresponding XP spectra for this specific sample that well resembles our previously published results. The x-axis intercept of the red dashed line at ~ 17 eV vs the Fermi energy of Au, $E_{F,Au} \equiv 0$ eV reveals the secondary electron cutoff energy, E_{SEC} from which we derive work function values $\phi \equiv h\nu - E_{SEC}$. For the sample in Figure 4, $\phi = 4.03$ eV, while for the nine samples scanned, the average was $\phi = 4.0$ eV with a standard deviation of 0.3 eV.

Consideration of band-edge positioning and previous UV-Vis data aid in the interpretation of Fermi regions for the UP spectra of the films studied. Revealed by the representative ×16-scaled Fermi region inset in Figure 4, a green-dashed linear fit of the UP spectrum corresponds to the Fermi-level energy vs the valence band-maximum energy, $E_{\mbox{\tiny F}}$ – $E_{\mbox{\tiny VBM}}$ = 3.74 eV. Interestingly, the green-dashed linear fit reveals a region of photoelectron signal that may be alternatively ascribed to photoemission from near-valence band-edge states or may be fitted as the correct valence-band position itself. Considering the possibility of a different valence band position, fitting a line above the gray-shaded photoelectron counts at binding energies between 4 and 1 eV would yield $E_F - E_{VBM} =$ 1.65 eV. Figure S2 in the Supporting Information section presents a fit of near-valence edge photoemission such that E_F $-E_{VBM} = 1.65$ eV that in concert with $E_g = 4.0$ eV from Figure

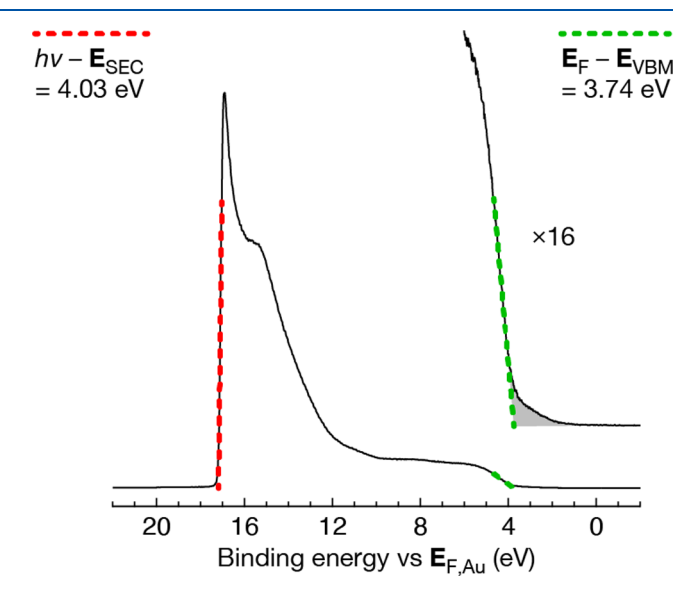


Figure 4. UP spectrum of a LiCl-rinsed 1DL thin film. Linear dashed fits reveal the secondary electron cutoff energy \mathbf{E}_{SEC} (red dashed line) and the binding energy of the valence band maximum, \mathbf{E}_{VBM} , relative to its Fermi energy, \mathbf{E}_F . The inset spectrum on the right represents a magnified view to clarify the near-Fermi-edge density of states. Grayshaded photoelectron counts at energies between \mathbf{E}_{VBM} and \mathbf{E}_F are ascribed to defect states within the band gap.

2C and $\phi=4.0$ eV implies a conduction band minimum E_{CBM} of -1.7 eV vs the vacuum energy level, $E_{\rm vac}.$ Such a high conduction band maximum and small electron affinity should not be realistic for quantum-confined titanium oxides, 27 which implies that $E_F-E_{VBM}=1.7$ eV represents an erroneous fit to the Fermi edge region of the UP spectrum. Thus, the green fitted line represents a more realistic $E_F-E_{VBM}=3.74$ with the lower-binding-energy states above the gray region resulting from near-valence edge defects in the 1DL nanofilaments. For

the nine samples studied, $E_F - E_{VBM}$ demonstrated a 3.8 eV average with a 0.1 eV standard deviation. In concert with the UV–Vis absorption data, the UP spectra determine the bandedge positioning presented in the Discussion section below to elucidate our observed transient absorption behavior of our films.

In the absence of LiCl rinsing, UP spectra on films that are similar to that used for Figure 3A demonstrate work function energies $\phi = 2.6$ eV with a standard deviation of 0.5 eV that we ascribe as erroneously low and an artifact of TMA+ cations sitting above surface Ti-O- states on 1DL nanofilaments yielding a large interfacial dipole normal to the surface. Conversely, LiCl rinsing may obviate interfacial dipoles as the small Li⁺ may reside between adjacent Ti-O⁻ sites that yield no significant dipole aligned with the surface normal angle. The exact nature of the cation-surface interaction remains the subject of ongoing study as surface dipoles demonstrate strong influences on charge transfer from the valence band relevant to electrochemistry and catalysis, 28 but smaller effects on charge transfer from core levels in photoelectron spectra.²⁹ However, we perform all subsequent transient absorption studies using LiCl-rinsed films.

Transient absorption (TA) following sub-gap optical excitation provides additional insight into the nature and lifetimes of resulting photoexcitations and energy levels for films of LiCl-rinsed 1DL. Figure 5 shows transient absorption kinetics and spectra following excitation with 400 nm (3.1 eV), $63.7 \mu \text{J}$ cm⁻² fluence, 90 fs pulses. Qualitatively similar results

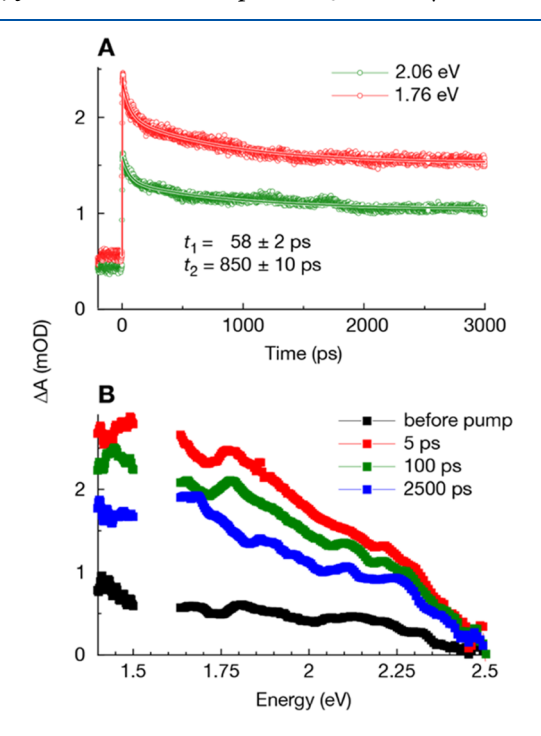


Figure 5. Transient absorption spectroscopy of thin 1DL films. Excited-state absorption taken at 700 nm (1.77 eV) and 600 nm (2.06 eV) in frame (A) are well described by the double-exponential-decay fits in solid lines. Transient absorption spectra in frame (B), both prior to pump arrival (black) as well as following 5 ps (red), 100 ps (green), and 2.5 ns (blue) following excitation with 400 nm optical pulses. The nonzero differential absorption before pump arrival (black) indicates residual photoinduced absorption that persists longer than the time between two consecutive excitation pulses (10 $\mu \rm s$).

exist for lower energy, 485 nm (2.65 eV) excitation, but stronger pump absorption at 3.1 eV improved the signal/noise ratios. Importantly, sub-gap photoexcitation results in broadband, excited-state absorption (ESA) that extends beyond our experimental window of ~1.4-2.5 eV. Photoexcited absorption is long-lived, as demonstrated by the excited absorption decay traces taken at 700 nm (1.76 eV) as well as 600 nm (2.06 eV). The behavior of excited-state absorption is essentially independent of the probe wavelength, suggesting that the broad photoinduced absorption arises from photoexcitation states that have the same origin. Decay traces can be fitted to a double-exponential decay with a short decay time of τ_1 = 58 ± 2 ps and a longer decay of τ_2 = 850 ± 10 ps. In addition, there is a much slower decay component that cannot be accurately determined, given our experimental time window. Excited-state absorption signals decay only to >50% of the peak value by 3 ns and persist for μ s timescales, as evidenced by a nonzero signal at negative times or residual signal that does not fully recover between the time window of 10 μ s between the two consecutive pump pulses.

4. DISCUSSION

Both static and transient optical absorption spectroscopy reveal that our 1DL nanostructures absorb light across the visible range, owing to the presence of sub-gap states, as illustrated in Figure 5. However, interpretation of transient absorption results presents challenges both due to the underexplored nature of 1DLs and the broad range of transient absorption results for titanium oxide in the literature. Elsewhere, TA experiments with a 350 nm (3.54 eV) pump at fluences up to 200 μ J cm⁻² found a 3.0 ns transient absorption decay time in single-crystal anatase but a significantly longer 48 ns decay time in single-crystal rutile ascribed to optical absorption from photoexcited holes.³⁰ The presently quantified τ_2 lifetime of 850 ps in the 1DL films demonstrates significantly closer agreement with the TA results for single-crystal anatase however that comparison does not include the non-quantified, long-lived TA lifetime that yields non-zero absorption at negative times in Figure 5. Conversely, experiments on nanocrystalline TiO2 films demonstrated transient absorption behavior dominated by an intraband relaxation of hot holes with a lifetime longer than 100 ps following 266 nm photoexcitation. 31 Experiments on nanocrystalline ${\rm TiO_2}$ with a 355 nm pump demonstrated transient absorption decay lifetimes of 500 ps for both a 1.54 eV probe for surface-trapped electrons and a 0.50 eV probe of bulk electrons.³² For nanocrystalline TiO₂ films, high, 14 mJ cm⁻² excitation fluences at 3.49 eV yielded transient absorption lifetimes of a few ns at probe energies between 0.95 and 1.55 eV, 33 while recent results establish a pump-fluence dependence on surface reorganization with profound impacts for the transient absorption dynamics.³⁴ The Figure 2 structure of this material and correlations of spectroscopic results with its structure and defects remain the subject of ongoing efforts. The recently updated structure³ should enable computational insight into the interplay between states, defects, band structures, and the resulting carrier dynamics for this lepidocrocite-like titanium dioxide material.

Figure 6 presents a band energy diagram consistent with the UV–Vis, ultraviolet photoelectron, and transient absorption spectroscopies on the left as well as band edges for selected titanium oxide materials from the literature on the right. The UPS-determined work function yields $E_F = -4.0 \pm 0.3$ eV vs

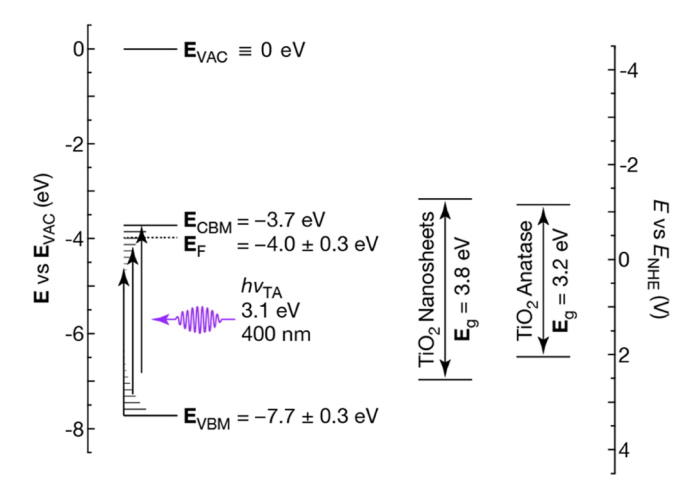


Figure 6. UV—Vis and UP spectra yield band-edge positions (left) for Ti-based 1DL nanofilaments vs the vacuum energy level, \mathbf{E}_{VAC} . Observation of sub-gap excitation in transient absorption experiments implies the presence of intra-gap states that are consistent with near-valence edge defects observed in UP spectra and near-conduction-edge defects that are ascribable to the established Ti^{3+} for Ti-based 1DL nanofilaments. Comparison with literature reports of electrochemistry-derived band edges for nanosheet (middle) and anatase TiO_2 (right) from ref 37 support both the large quantum confinement in 1DLs and established offsets when comparing work functions derived from ultrahigh vacuum vs electrochemical methods per ref 39.

E_{VAC}, while the Fermi edge and Tauc-determined band gap position the valence and conduction band edges at -7.7 ± 0.3 and -3.7 ± 0.3 eV, respectively. We consider the position of the Fermi energy relative to the band-edge positioning to indicate strong but not degenerate n-type doping with the Fermi level 0.2–0.3 eV, or roughly 10 k_BT , more negative than the conduction band edge at the standard-state temperature. Absorption of 400 nm (3.1 eV) light implies the existence of additional states in addition to the bands themselves. We therefore hypothesize that sub-gap states are associated with electronic defects that may result from surface states. Observation of photoelectron counts at binding energies in between the valence band edge and the Fermi level implies the existence of defect states at least near the valence band. Such near-valence-band defect states are well precedented in the titania literature. 35 In addition to near-valence-band defect states, we cannot rule out the existence of near-conductionband-edge defect states, such as those that arise from Ti³⁺ cations and/or oxygen vacancies as well. 36 Such Ti^{3+} defects and oxygen vacancies are notable for their implication in "black" TiO₂ in the literature²⁰ and may explain the black coloration of the presently studied material. Thus, the observation of long-lived photoexcitations that yield the excited-state absorption observed in Figure 5 may be valence-defect, defect-defect, or defect-conduction transitions on the band diagram shown on the lefthand side of Figure 6. Exploration of the nature of these transitions and implications for the exceptional catalytic properties of 1DL nanofilaments remain the subject of ongoing study.

Comparison of the band edges with other TiO_2 materials further highlights the unique nature of our films. The middle and righthand side band edges respectively represent bandedge positions for nanosheet TiO_2 and bulk anatase as derived via electrochemical methods.³⁷ In Figure 6, we relate electrochemical potentials, E, to energies, E, via $-qE_{\rm NHE}$ =

 $E_{\rm NHE} = -4.44~{\rm eV}$ vs $E_{\rm vac}$ under standard conditions based on IUPAC recommendations. ³⁸ Comparing with the 3.8 eV band gap for the nanosheet films, ³⁷ our films demonstrate a higher degree of quantum confinement resulting in their ~4.0 eV band gap. Notably, the band-edge positions for the literature ${\rm TiO_2}$ reports in the middle and righthand side are offset as compared to the presently reported band edges for 1DL films on the lefthand side of Figure 6. However, such offsets are consistent with discrepancies between work functions acquired via ultrahigh vacuum vs electrochemical methods. ³⁹

In summary, we report the properties of photoexcitations in a new class of lepidocrocite-like titania-based nanostructures and relate the nature of sub-gap excitation to band and defect structures. Important questions remain underlying the mechanism of synthesis, the presence of chemical defects, as well as the nature of light-emitting states. However, the scalability and ease of synthesis using common solvents such as TMAOH and precursors such as TiC, TiB_2 , etc., their extraordinary surface area, and exceptionally long-lived photoexcitations that can be excited with visible, sub-gap light raise exciting prospects of application in solar energy conversion and visible optoelectronic devices, among others.

ASSOCIATED CONTENT

Supporting Information

The Supporting Information is available free of charge at https://pubs.acs.org/doi/10.1021/acs.jpcc.2c06719.

Raw absorbance spectrum for the Tauc plot in Figure 2C as well as indirect Tauc, direct Tauc, and Cody plots for the absorbance data (Figure S1) and fits of the valence region of the UP spectrum in Figure 4 in support of the chosen fitting regime (Figure S2) (PDF)

AUTHOR INFORMATION

Corresponding Authors

Ronald L. Grimm – Department of Chemistry & Biochemistry, Worcester Polytechnic Institute, Worcester, Massachusetts 01609, United States; oocid.org/0000-0003-0407-937X; Email: grimm@wpi.edu

Lyubov V. Titova — Department of Physics, Worcester Polytechnic Institute, Worcester, Massachusetts 01609, United States; oorcid.org/0000-0002-2146-9102; Email: ltitova@wpi.edu

Authors

Erika Colin-Ulloa – Department of Physics, Worcester Polytechnic Institute, Worcester, Massachusetts 01609, United States

Julia L. Martin — Department of Chemistry & Biochemistry, Worcester Polytechnic Institute, Worcester, Massachusetts 01609, United States; orcid.org/0000-0001-7609-9922

Ryan J. Hanna — Department of Physics, Worcester Polytechnic Institute, Worcester, Massachusetts 01609, United States; Department of Chemistry & Biochemistry, Worcester Polytechnic Institute, Worcester, Massachusetts 01609, United States

Michelle H. Frasch – Department of Chemistry & Biochemistry, Worcester Polytechnic Institute, Worcester, Massachusetts 01609, United States

Rebecca R. Ramthun – Department of Chemistry & Biochemistry, Worcester Polytechnic Institute, Worcester, Massachusetts 01609, United States

- Hussein O. Badr Department of Material Science and Engineering, Drexel University, Philadelphia, Pennsylvania 19104, United States
- Joshua R. Uzarski Soldier Protection Directorate, US Army Development Command Soldier Center, Natick, Massachusetts 01760, United States
- Michel W. Barsoum Department of Material Science and Engineering, Drexel University, Philadelphia, Pennsylvania 19104, United States; orcid.org/0000-0001-7800-3517

Complete contact information is available at: https://pubs.acs.org/10.1021/acs.jpcc.2c06719

Author Contributions

¹Denotes equal contribution.

Notes

The authors declare no competing financial interest.

ACKNOWLEDGMENTS

This work was supported by the DEVCOM Soldier Center Inhouse Independent Laboratory (ILIR) basic research program. This manuscript was approved for public release by the DEVCOM Soldier Center Public Affairs Office, PAO #PR2023_54227. NSF DMR-2018326 funded the ultrafast transient absorption spectrometer.

REFERENCES

- (1) Badr, H. O.; El-Melegy, T.; Carey, M.; Natu, V.; Hassig, M. Q.; Johnson, C.; Qian, Q.; Li, C. Y.; Kushnir, K.; Colin-Ulloa, E.; et al. Bottom-Up, Scalable Synthesis of Anatase Nanofilament-Based Two-Dimensional Titanium Carbo-Oxide Flakes. *Mater. Today* **2022**, *54*, 8–17.
- (2) Badr, H. O.; Montazeri, K.; El-Melegy, T.; Natu, V.; Carey, M.; Gawas, R.; Phan, P.; Qian, Q.; Li, C. Y.; Wiedwald, U.; et al. Scalable, Inexpensive, One Pot, Synthesis of Crystalline Two-dimensional Birnessite Flakes. *Matter* **2022**, *4*, 2365–2381.
- (3) Badr, H. O.; Lagunas, F.; Autrey, D. E.; Autry, D.; Cope, J.; Kono, T.; Torita, T.; Klie, R.; Klie, R. F.; Hu, Y.-J.; Hu, Y. J.; Barsoum, M. W. On the Structure of One-Dimensional ${\rm TiO}_2$ Lepidocrocite. *Matter* **2023**, *6*, 128–141.
- (4) Sorrentino, A. L.; Serrano, G.; Poggini, L.; Cortigiani, B.; El-Kelany, K. E.; D'Amore, M.; Ferrari, A. M.; Atrei, A.; Caneschi, A.; Sessoli, R.; Mannini, M. Quasi-Hexagonal to Lepidocrocite-like Transition in TiO₂ Ultrathin Films on Cu(001). *J. Phys. Chem. C* **2021**, *125*, 10621–10630.
- (5) Wang, S. L.; Luo, X.; Zhou, X.; Zhu, Y.; Chi, X.; Chen, W.; Wu, K.; Liu, Z.; Quek, S. Y.; Xu, G. Q. Fabrication and Properties of a Free-Standing Two-Dimensional Titania. *J. Am. Chem. Soc.* **2017**, *139*, 15414–15419.
- (6) Liao, T.; Sun, Z.; Dou, S. X. Theoretically Manipulating Quantum Dots on Two-Dimensional TiO₂ Monolayer for Effective Visible Light Absorption. ACS Appl. Mater. Interfaces **2017**, *9*, 8255–8262.
- (7) Sheng, L.; Liao, T.; Kou, L.; Sun, Z. Single-Crystalline Ultrathin 2D TiO₂ Nanosheets: A Bridge Towards Superior Photovoltaic Devices. *Mater. Today Energy* **2017**, *3*, 32–39.
- (8) Wang, A. S. D.; Sasaki, T. Titanium Oxide Nanosheets: Graphene Analogues with Versatile Functionalities. *Chem. Rev.* **2014**, 114, 9455–9486.
- (9) Monticone, S.; Tufeu, R.; Kanaev, A. V.; Scolan, E.; Sanchez, C. Quantum Size Effect in TiO₂ Nanoparticles: Does it Exist? *Appl. Surf. Sci.* **2000**, *162*–*163*, 565–570.
- (10) Schneider, J.; Matsuoka, M.; Takeuchi, M.; Zhang, J.; Horiuchi, Y.; Anpo, M.; Bahnemann, D. W. Understanding TiO₂ Photocatalysis: Mechanisms and Materials. *Chem. Rev.* **2014**, *114*, 9919–9986.
- (11) Fujishima, A.; Rao, T. N.; Tryk, D. A. Titanium Dioxide Photocatalysis. *J. Photochem. Photobiol.*, C **2000**, 1, 1–21.

- (12) Kuvarega, A. T.; Mamba, B. B. TiO₂-based Photocatalysis: Toward Visible Light-Responsive Photocatalysts Through Doping and Fabrication of Carbon-Based Nanocomposites. *Crit. Rev. Solid State Mater. Sci.* **2017**, 42, 295–346.
- (13) Wang, H.; Lewis, J. P. Effects of Dopant States on Photoactivity in Carbon-Doped TiO₂. *J. Phys.: Condens. Matter* **2005**, *17*, L209–L213
- (14) Irie, H.; Watanabe, Y.; Hashimoto, K. Carbon-Doped Anatase TiO_2 Powders as a Visible-Light Sensitive Photocatalyst. *Chem. Lett.* **2003**, *32*, 772–773.
- (15) Di Valentin, C.; Pacchioni, G.; Selloni, A. Theory of Carbon Doping of Titanium Dioxide. *Chem. Mater.* **2005**, *17*, 6656–6665.
- (16) Varsano, D.; Giorgi, G.; Yamashita, K.; Palummo, M. Role of Quantum-Confinement in Anatase Nanosheets. *J. Phys. Chem. Lett.* **2017**, *8*, 3867–3873.
- (17) Migas, D. B.; Filonov, A. B.; Borisenko, V. E.; Skorodumova, N. V. Orientation Effects in Morphology and Electronic Properties of Anatase ${\rm TiO_2}$ One-Dimensional Nanostructures. I. Nanowires. *Phys. Chem. Chem. Phys.* **2014**, *16*, 9479–9489.
- (18) Migas, D. B.; Filonov, A. B.; Borisenko, V. E.; Skorodumova, N. V. Orientation Effects in Morphology and Electronic Properties of Anatase ${\rm TiO_2}$ One-Dimensional Nanostructures. II. Nanotubes. *Phys. Chem. Chem. Phys.* **2014**, *16*, 9490–9498.
- (19) Tosoni, S.; Pacchioni, G. Hydrogen Adsorption on Free-Standing and Ag-Pt Supported TiO₂ Thin Films. *J. Phys. Chem. C* **2019**, *123*, 7952–7960.
- (20) Rajaraman, T. S.; Parikh, S. P.; Gandhi, V. G. Black TiO₂: A Review of its Properties and Conflicting Trends. *Chem. Eng. J.* **2020**, 389, No. 123918.
- (21) Carl, A. D.; Kalan, R. E.; Obayemi, J. D.; Zebaze Kana, M. G.; Soboyejo, W. O.; Grimm, R. L. Synthesis and Characterization of Alkylamine-Functionalized Si(111) for Perovskite Adhesion With Minimal Interfacial Oxidation or Electronic Defects. *ACS Appl. Mater. Interfaces* **2017**, *9*, 34377–34388.
- (22) Fairley, N. Peak Fitting in XPS, 2015. http://www.casaxps.com/help manual/manual updates/peak fitting in xps.pdf.
- (23) Shirley, D. A. High-Resolution X-Ray Photoemission Spectrum of the Valence Bands of Gold. *Phys. Rev. B* **1972**, *5*, 4709–4714.
- (24) Tougaard, S. Formalism for Quantitative Surface Analysis by Electron Spectroscopy. J. Vac. Sci. Technol., A 1990, 8, 2197–2203.
- (25) Jansson, C.; Hansen, H. S.; Yubero, F.; Tougaard, S. Accuracy of the Tougaard Method for Quantitative Surface Analysis. Comparison of the Universal and REELS Inelastic Cross Sections. *J. Electron Spectrosc. Relat. Phenom.* **1992**, *60*, 301–319.
- (26) Nyholm, R.; Martensson, N.; Lebugle, A.; Axelsson, U. Auger and Coster-Kronig Broadening Effects in the 2p and 3p Photoelectron Spectra From the Metals ²²Ti-³⁰Zn. *J. Phys. F: Met. Phys.* **1981**, *11*, 1727–1733.
- (27) Scanlon, D. O.; Dunnill, C. W.; Buckeridge, J.; Shevlin, S. A.; Logsdail, A. J.; Woodley, S. M.; Catlow, C. R. A.; Powell, M. J.; Palgrave, R. G.; Parkin, I. P.; et al. Band alignment of rutile and anatase TiO₂. *Nat. Mater.* **2013**, *12*, 798–801.
- (28) Walter, M. G.; Warren, E. L.; McKone, J. R.; Boettcher, S. W.; Mi, Q.; Santori, E. A.; Lewis, N. S. Solar Water Splitting Cells. *Chem. Rev.* **2010**, *110*, 6446–6473.
- (29) Gleason-Rohrer, D. C.; Brunschwig, B. S.; Lewis, N. S. Measurement of the Band Bending and Surface Dipole at Chemically Functionalized Si(111)/Vacuum Interfaces. *J. Phys. Chem. C* **2013**, 117, 18031–18042.
- (30) Yamada, Y.; Kanemitsu, Y. Determination of electron and hole lifetimes of rutile and anatase TiO_2 single crystals. *Appl. Phys. Lett.* **2012**, *101*, No. 133907.
- (31) Tamaki, Y.; Furube, A.; Katoh, R.; Murai, M.; Hara, K.; Arakawa, H.; Tachiya, M. Trapping dynamics of electrons and holes in a nanocrystalline TiO₂ film revealed by femtosecond visible/near-infrared transient absorption spectroscopy. C. R. Chim. **2006**, *9*, 268–274
- (32) Tamaki, Y.; Furube, A.; Murai, M.; Hara, K.; Katoh, R.; Tachiya, M. Dynamics of efficient electron-hole separation in TiO₂

nanoparticles revealed by femtosecond transient absorption spectroscopy under the weak-excitation condition. *Phys. Chem. Chem. Phys.* **2007**, *9*, 1453–1460.

- (33) Katoh, R.; Murai, M.; Furube, A. Transient absorption spectra of nanocrystalline TiO₂ films at high excitation density. *Chem. Phys. Lett.* **2010**, 500, 309–312.
- (34) Schneider, J.; Bahnemann, D. Strong Transient Absorption of Trapped Holes in Anatase and Rutile TiO₂ at High Laser Intensities. *J. Phys. Chem. C* **2018**, *122*, 13979–13985.
- (35) Samsudin, E. M.; Abd Hamid, S. B. Effect of Band Gap Engineering in Anionic-Doped TiO₂ Photocatalyst. *Appl. Surf. Sci.* **2017**, 391, 326–336.
- (36) Choudhury, B.; Choudhury, A. Oxygen Defect Dependent Variation of Band Gap, Urbach Energy and Luminescence Property of Anatase, Anatase–Rutile Mixed Phase and of Rutile Phases of TiO₂ Nanoparticles. *Phys. E* **2014**, *56*, 364–371.
- (37) Sakai, N.; Ebina, Y.; Takada, K.; Sasaki, T. Electronic Band Structure of Titania Semiconductor Nanosheets Revealed by Electrochemical and Photoelectrochemical Studies. *J. Am. Chem. Soc.* 2004, 126, 5851–5858.
- (38) Trasatti, S. The Absolute Electrode Potential: An Explanatory Note (Recommendations 1986). *Pure Appl. Chem.* **1986**, *58*, 955–966.
- (39) Mansfeldova, V.; Zlamalova, M.; Tarabkova, H.; Janda, P.; Vorokhta, M.; Piliai, L.; Kavan, L. Work Function of TiO₂ (Anatase, Rutile, and Brookite) Single Crystals: Effects of the Environment. *J. Phys. Chem. C* **2021**, *125*, 1902–1912.

TRecommended by ACS

Characterization of Planar Defect in Layered Perovskite Photocatalyst $Y_2Ti_2O_5S_2$ by Electron Microscopy and First-Principles Calculations

Mamiko Nakabayashi, Seiichiro L. Ten-no, et al.

APRIL 14, 2023

THE JOURNAL OF PHYSICAL CHEMISTRY C

READ 🗹

Revisiting the Crystal Structure of Layered Oxychalcogenides Ln,O,S, (Ln = La, Pr, and Nd)

Louis-Béni Mvélé, Laurent Cario, et al.

MAY 03, 2023

INORGANIC CHEMISTRY

READ 🗹

First-Principles Thermodynamics of CsSnI₃

Lorenzo Monacelli and Nicola Marzari

FEBRUARY 06, 2023

CHEMISTRY OF MATERIALS

READ 🗹

Versatile Interplay of Chalcogenide and Dichalcogenide Anions in the Thiovanadate $Ba_7S(VS_3O)_2(S_2)_3$ and Its Selenide Derivatives: Elaboration and DFT Meta-GGA S...

Batoul Almoussawi, Houria Kabbour, et al.

MAY 02, 2023

ACS ORGANIC & INORGANIC AU

READ 🗹

Get More Suggestions >